

## Transforming Fullerene into Graphene Quantum Dots

Jiong Lu, Pei Shan Emmeline Yeo, Chee Kwan Gan, Ping Wu and Kian Ping Loh<sup>★</sup>

<sup>★</sup>email: chmlhkp@nus.edu.sg

### Contents

**Figure S1** | Transformation of 1.2 ML C<sub>60</sub> film on Ru(0001) into a single layer graphene at 1200 K for 5 minutes.

**Figure S2** | STM topography images shows typical large sized graphene nanoislands formed.

**Figure S3** | STM simulations of a 2.7 nm quantum dot with H termination and without H termination.

**Figure S4** | Energy gap and size relation for GQDs. Inset: the equation from the least-squares fit.

**Figure S5** | Illustrate how to determine the energy gap of GQDs.

**Figure S6** | The constant current 3D STM images of C<sub>60</sub> molecules diffusion and sinking on Ru(0001); thermal fragmentation of C<sub>60</sub> and diffusion of C<sub>60</sub>-derived clusters at 650 K.

**Figure S7** | Experimental STM topography of irregular graphene islands grown from C<sub>2</sub>H<sub>4</sub> gas.

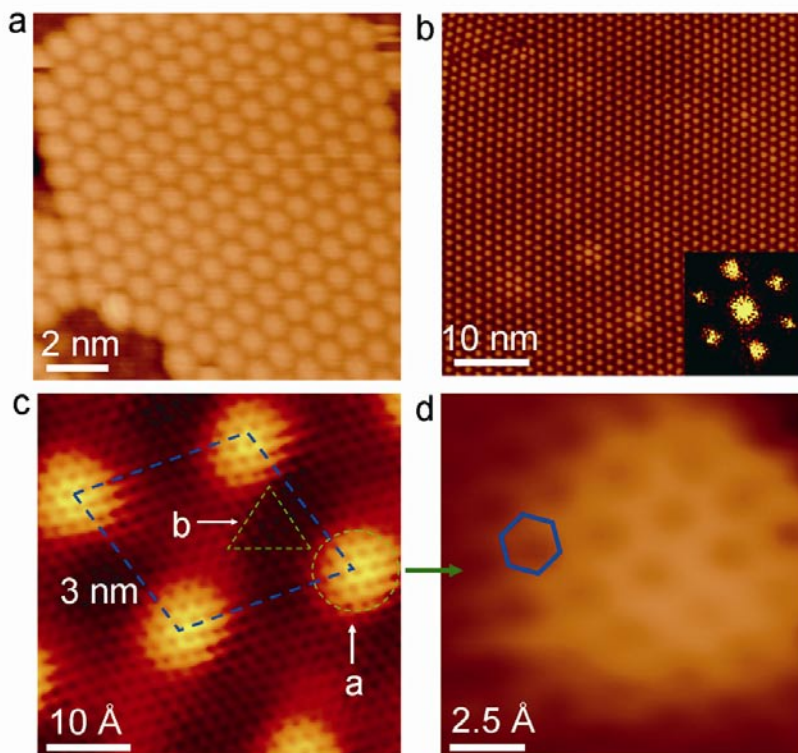
**Figure S8** | Experimental STM topography of irregular and large sized carbon clusters grown from C<sub>2</sub>H<sub>4</sub> gas.

**Figure S9** | Experimental STM topography of 5 nm GQDs with equilibrium shape observed at 1000 K.

**Table 1** | Different configurations of the hexagonal face of C<sub>60</sub> on the Ru(0001) substrate and their respective adsorption energies.

**Movie 1** | Dynamic STM video of C<sub>60</sub> molecules diffusion and sinking on Ru(0001) at 500-600 K.

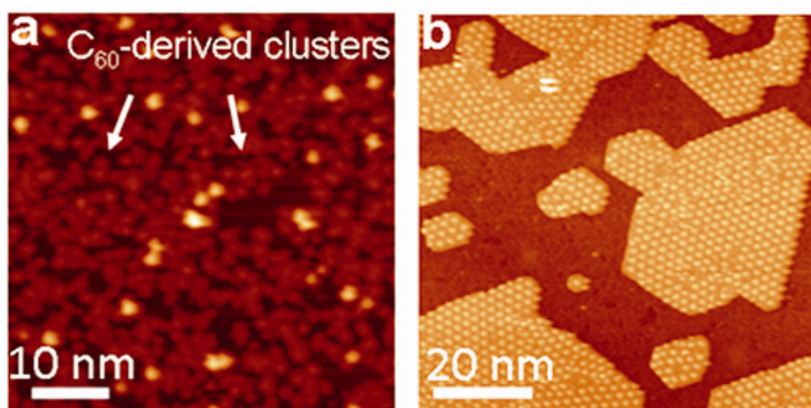
**Movie 2** | STM video of transferring non-equilibrium shaped GQDs to equilibrium shaped GQDs at 1000 K.



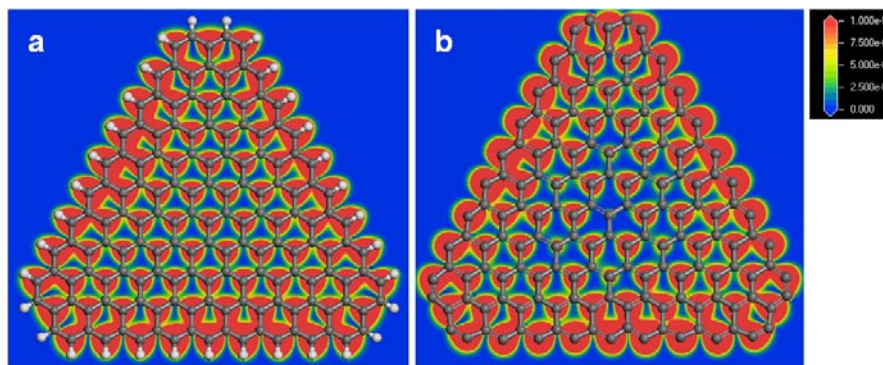
**Figure S1** | (a-d) Experimental STM topography results: (a) 1.2 ML  $C_{60}$  films deposited on the Ru (0001) surface (b) The hexagonal Moiré pattern of atomically flat graphene after annealing 1.2 ML  $C_{60}$  films at 1200 K; Fourier transforms (inset) of the image show 6-fold symmetry. (c) High-resolution image of the Moiré superstructure of the graphene layer. (d) Magnified view of the moiré maxima, showing a honeycomb lattice structure. Tunneling parameters: (a)  $V = 1.25$  V,  $I = 0.1$  nA; (b)  $V = 1.2$  V,  $I = 0.08$  nA; (c)  $V = 18$  mV,  $I = 0.5$  nA; (d)  $V = 18$  mV,  $I = 0.5$  nA.

Fig. S1 illustrates the transformation of 1.2 ML of  $C_{60}$  to a single layer of graphene on the Ru(0001) surface after annealing the sample at 1200 K for 5 minutes. The assembly of fullerene on Ru(0001) after annealing at 450 K produces a highly-ordered hexagonal arrangement (Fig. S1a). The monolayer, large-sized graphene adopts an incommensurate moiré structure on the Ru(0001) surface (Fig. S1b), due to the lattice mismatch between graphene and Ru(0001)<sup>1-5</sup>. Fourier transforms of the STM image (inset in Fig. S1b) indicates that the graphene adlayer exhibits an ordered superstructure with a 6-fold symmetry with a lattice constant of 30 Å, suggesting that a (12 × 12) graphene supercell sits on a (11 × 11) Ru surface supercell. For large-sized graphene on Ru(0001), the symmetric honeycomb graphene lattice expected for an

ideal, unperturbed graphene crystal<sup>6,7</sup> is observed in the moiré maxima (the circled part in Fig. S1c) as shown in Fig. S1d. In these regions, the graphene sheet is lifted higher above the ruthenium atoms and couples weakly to the substrate<sup>1,5</sup>. In the moiré valley (the triangular part in Fig. S1c), the 2.5 Å triangular lattice pattern was observed due to the strong, covalent interaction with the Ru substrate, which resulted in the breakage of the symmetry in the two graphene sublattices. Therefore, only three of the six carbon atoms in each hexagonal ring were imaged (the so-called “3-for-6” pattern).



**Figure S2** | (a) STM topography images of C<sub>60</sub> fragments formed by the decomposition of 0.5 ML C<sub>60</sub> at 675-700 K. (b), typical large sized graphene nanoislands formed after annealing the sample above 800 K. Tunneling parameters: (a)  $V = 1.25$  V,  $I = 0.2$  nA; (b)  $V = 1.25$  V,  $I = 0.1$  nA.



**Figure S3** | STM simulations a 2.7 nm quantum dot with H termination (**a**) and without H termination (**b**) at 0.3 eV below the Fermi level.

### “3-for-6” pattern

The “3-for-6” lattice pattern for monolayer GQDs is identical to the triangular symmetry observed in bilayer graphene and graphite<sup>8</sup>. Various reasons have been invoked to explain the “3-for-6” pattern, including local strain effect<sup>9</sup>, or edge-induced quantum interference<sup>10</sup>. For large graphene sheets adsorbed on the Ru(0001) surface, the symmetry of the two C atoms in the bipartite lattice is broken because they are located on different sites on the Ru(0001) substrate. Hence, only the atoms of one particular sublattice are imaged by STM. In the area where the graphene is buckled and not interacting with the substrate, the 6-fold symmetry of the lattice is restored and both C atoms are imaged (Fig. S1). To address why the “3-for-6” pattern is observed in the buckled regions of the triangular GQDs where there is no interaction with the Ru substrate, the local density of states of a 2.7 nm triangular GQD with H or without H on the edge, similar to the one we observed experimentally, is calculated. Triangular GQDs exhibit the “3-for-6” image even without the influence of the substrate (Fig. S3) because of the topological frustration of the  $\pi$ -bonds due to the finite size of the GQD. This topological frustration results in the appearance of spin states near the Fermi level that are localized on one particular sublattice of the GQD<sup>11</sup>.

Hence, the local density of states of only one particular sublattice is imaged under STM and this result in the “3-for-6” image. The dangling bonds at the edges of the GQD are partially quenched by interactions with the Ru substrate. This bonding situation is likely to be between the case of a GQD fully terminated by H, and the case where the GQD is not terminated by H at all. In either of these situations however, the “3-for-6” image is still seen, as our results show.

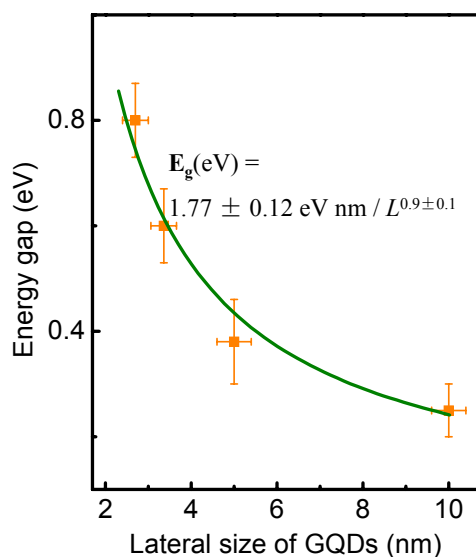


**Figure S4** | Energy gap and size relation for GQDs. Inset: the equation from the least-squares fit.

### Determining the energy gap of GQDs

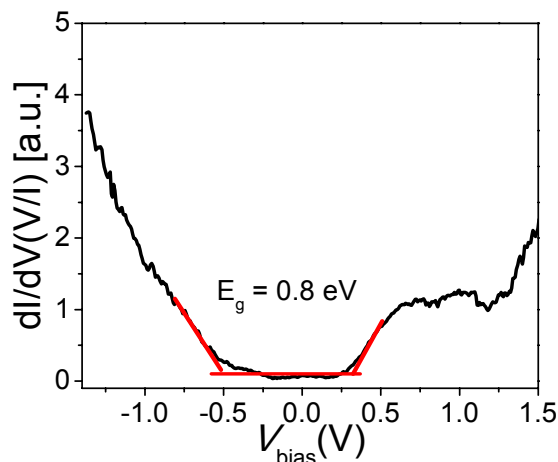


**Figure S5** | Illustrate how to determine the energy gap of GQDs.

The energy gap was determined following the methods which have been reported previously<sup>10,12</sup>. The data (I-V) is an arithmetic average of values measured at 20-70 grid points on the GQDs (depending on the size of GQDs). The red lines are used to fit the region of constant conductivity and the onset of the valence band and conduction band edges. The intersection of the lines determines the valence and conduction band edges, respectively, which shows an energy gap of 0.8 eV. We have reproduced the experimental spectra by sputtering the tip in-situ and also done the same measurement from different tips, thereby ruling out any contribution arising from tip artifacts. The size of GQDs was determined from experiment by averaging the minimum and maximum lateral dimension. Since the GQDs have a regular shape, we can calculate the surface area of different shaped GQDs and its corresponding diameter of the round-shaped dots with the same surface area. The sizes determined from the second method also roughly match the average value of the minimum and maximum lateral dimension.

### Determining the yield of GQDs and carbon clusters

Using the grid function in the scanning software, 9 surface areas ( $50 \times 50$  or  $100 \times 100 \text{ nm}^2$ , depending on the size of dots) were selected. The carbon clusters and GQDs were counted accordingly in each area. The same experiment was also repeated for three times and finally the averaged statistical results were obtained.

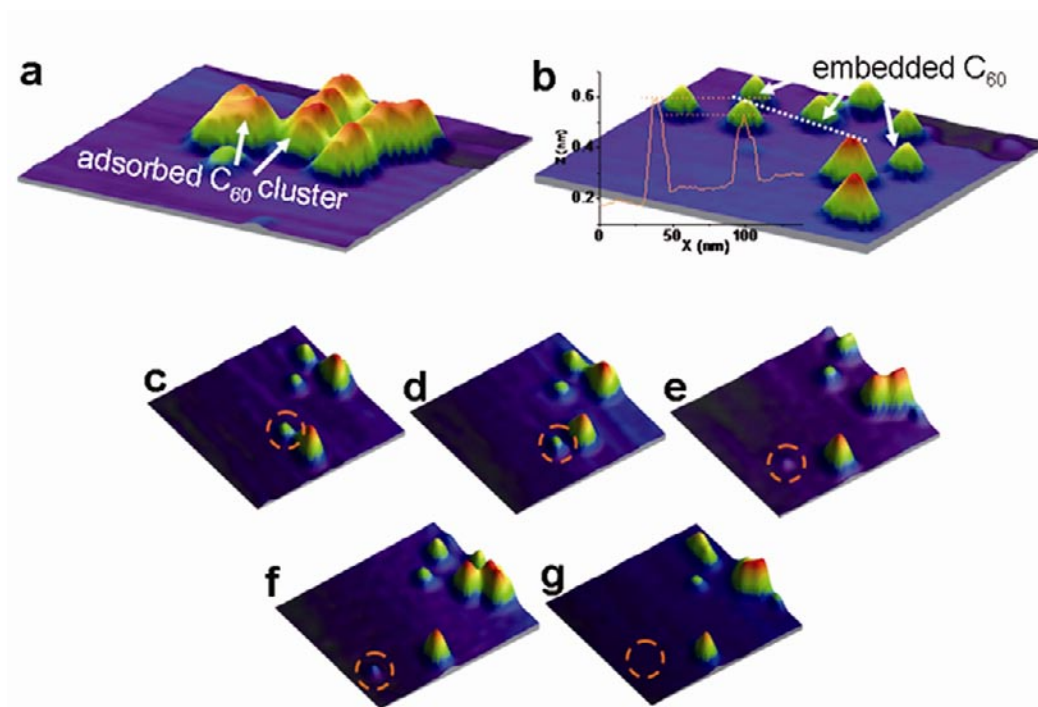


**Figure S6** | The constant current 3D  $24 \times 20 \text{ nm}^2$  STM images of C<sub>60</sub> molecules diffusion and sinking on Ru(0001). (a), At 500 K. (b), At 600 K. (c-g), Series of  $12 \times 10 \text{ nm}^2$  3D STM images monitoring the thermal fragmentation of C<sub>60</sub> (circled) and diffusion of C<sub>60</sub>-derived cluster at 650 K. Tunneling parameters: (a-g)  $V = 1.25 \text{ V}$ ,  $I = 0.1 \text{ nA}$ .

From the dynamic STM imaging, the molecular diffusion coefficient can be determined by tracking the position of the individual molecules, as reported previously<sup>13</sup>. The image acquisition time is varied according to the cluster mobilities, with values ranging from 10 to 20 sec per image ( $256 \times 256$  pixels). The typical carbon clusters derived from C<sub>60</sub> have a restricted surface mobility. The diffusion coefficient of the carbon clusters is dependent on the cluster size and temperature. The diffusion coefficient was determined in the range of  $10^{-15}$  to  $10^{-16} \text{ cm}^2\text{s}^{-1}$  in the imaging condition as shown above. At the same condition, the mobility of the carbon adatoms from C<sub>2</sub>H<sub>4</sub> is several orders of magnitude higher due to the low activation energy barrier of surface diffusion<sup>14</sup>, which is outside the recording speed of our STM.

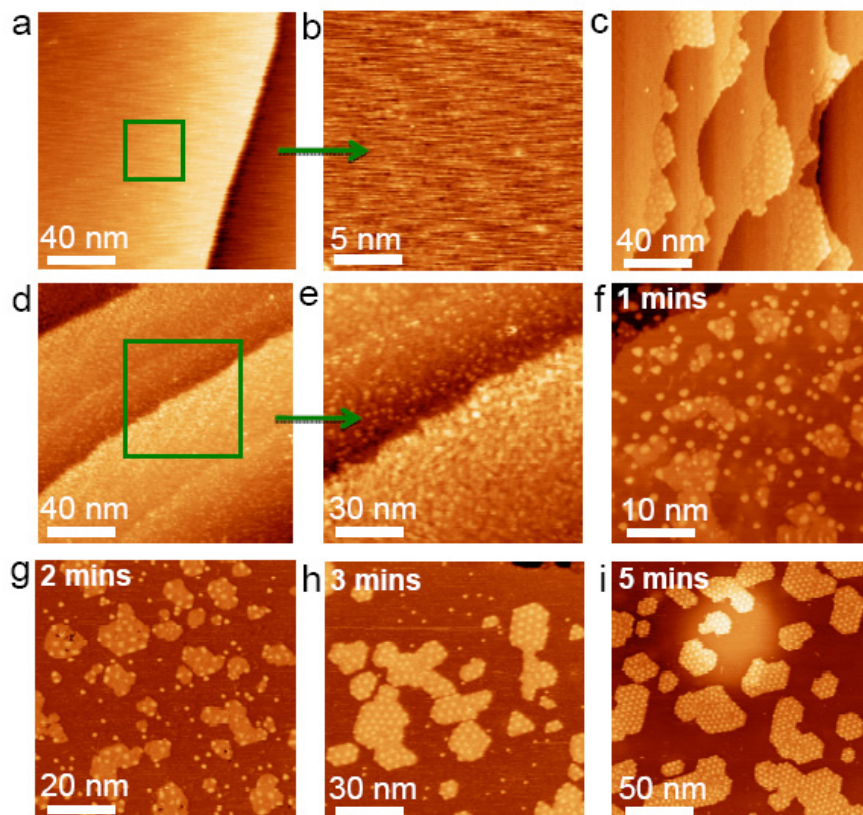


**Figure S7** | (a-i) Experimental STM topography of irregular shape graphene islands grown using  $C_2H_4$ . (a, b) Exposing sample to the ethylene flux for 10 s at  $1 \times 10^{-7}$  torr. (c) Nucleation of graphene islands starts from step edge after annealing the sample (a) at 725 K for 1 minute. (d, e) Exposing sample to the ethylene flux for 100 s at  $1 \times 10^{-7}$  torr. (f-i) The growth of irregular shaped graphene nanoislands at the expense of small carbon clusters with increasing annealing time (f) at 725 K (g-h) at 825 K. Tunneling parameters: (a-i)  $V = 1.25$  V,  $I = 0.1$  nA.

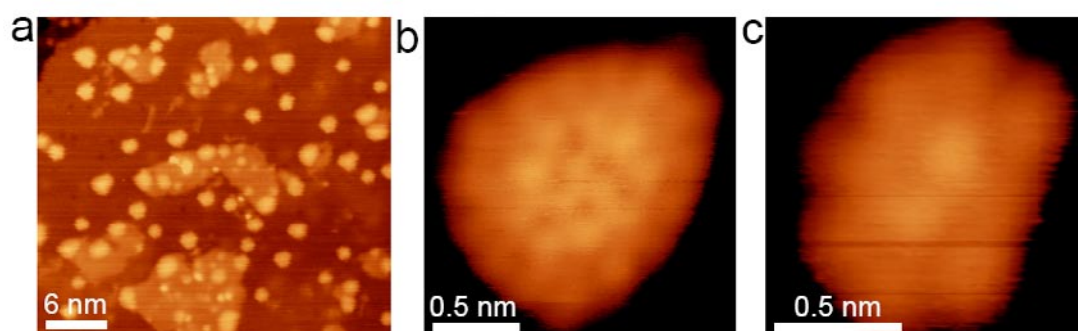
(1) STM studies indicate that these carbon adatoms produced from the dehydrogenation of  $C_2H_4$  are highly mobile out of the time scale of the STM scanning rate (Fig. S7b).

(2) At the low coverage  $C_2H_4$  ( $< 1$  L), nucleation of C adatom first occurs at the lower step edges of Ru, because catalytic dehydrogenation is more facile at these step edges and step geometry leads to the extra stability in the formation of carbon dimers<sup>15,16</sup>. However, the bonding strength is sufficient for  $C_{60}$  molecules to be anchored on the terraces ( $T < 500$ -550). After decomposition at elevated temperature, the  $C_{60}$ -derived clusters as the nucleation center incorporate arriving carbon clusters or migrate and

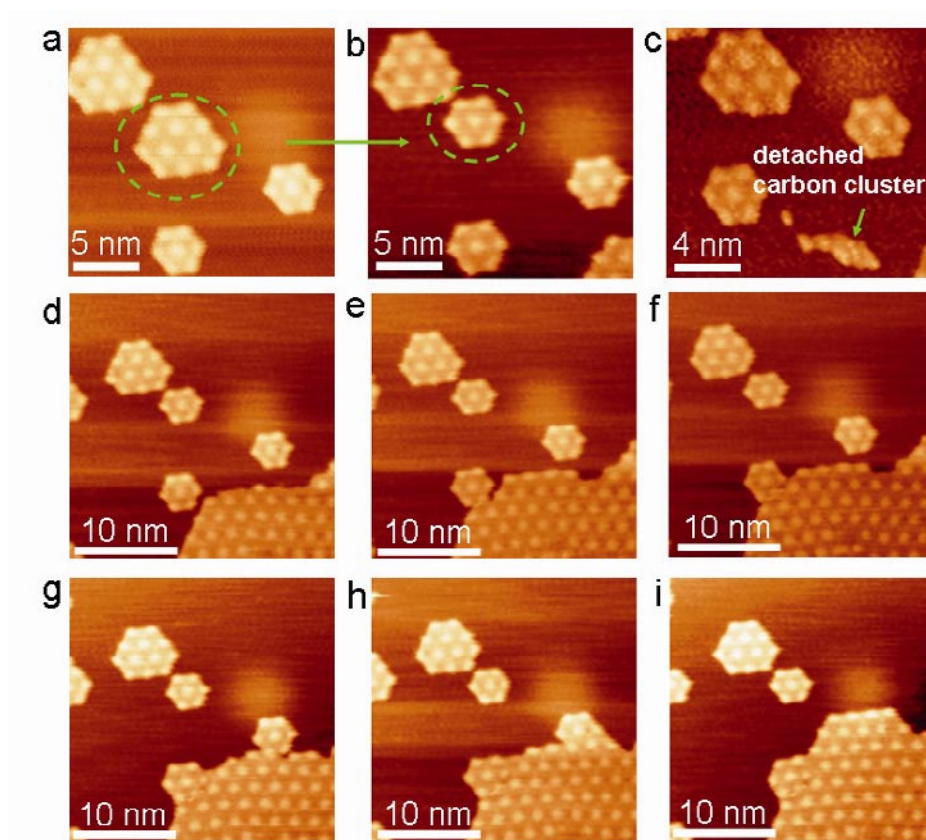


attach to the edge of existing islands. The restricted surface diffusion of those  $C_{60}$ -derived clusters ensures that the nucleation and growth of GQDs occur mainly on the terraces.

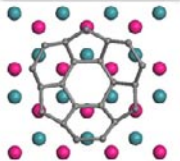
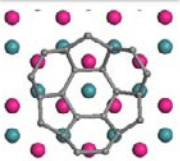
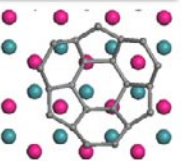
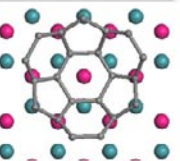
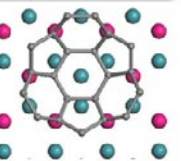
(3) With a high coverage of  $C_2H_4$ , the carbon clusters quickly lose their mobility after the fast collection of additional C monomers or dimers. The rapid edge growth by the condensation of C adatoms easily generates the large-sized islands with irregular growth shape by enlarging the existing one or coalescing with their neighbors. Thermally activated straightening of the edges of the graphene islands needs further raising of the temperature to initiate the diffusion and jumping of C atoms along the edges, which eventually results in the growth of even larger sized graphene islands (several tens of nanometers) possibly due to the accommodation of faster arriving C adatoms along with the Ostwald ripening process, where larger islands grow at the expense of the smaller ones (Fig. S7 f-i). In contrast, the decomposition of  $C_{60}$  in the wide range of 700-1000 K additionally slow the process of releasing carbon clusters and give rise a moderate growth speed, which will facilitate the formation of small-sized and well-separated GQDs towards its equilibrium shape.



**Figure S8** | (a-c) Experimental STM topography of typical irregular and large-sized carbon clusters grown from  $C_2H_4$  gas. Tunneling parameters: (a)  $V = 1.25$  V,  $I = 0.1$  nA, (b-c)  $V = 0.3$  V,  $I = 0.25$  nA.



**Figure S9** | (a-i) Experimental STM topography of 5 nm GQDs with equilibrium shape observed from annealing 0.2 ML  $C_{60}$  on Ru(0001) at 1000 K. (a, b) non-equilibrium GQDs evolved into equilibrium structure by detachment of edge carbon atoms. (c) The detached carbon atoms from non-equilibrium structures were captured. (d-i) The growth of 5 nm hexagonal GQDs cease and the shapes are retained on the surface unless they coalesce with the growing non-equilibrium islands.

Name	1) fcc	2) hcp	3) bridge	4) on-top	5) on-top_vac
Geometry					
Adsorption Energy (eV)	-7.695	-7.201	-7.793	-8.751	-9.077 <sup>a</sup> 1.361 <sup>b</sup>

● 1<sup>st</sup> layer Ru atom; ● 2nd layer Ru atom; ● C atom

**Table 1:** Different configurations of the hexagonal face of  $C_{60}$  on the Ru(0001) surface and their respective adsorption energies. The top hemisphere of the  $C_{60}$  is not shown for the sake of clarity. <sup>a</sup> Adsorption energy was calculated with respect to the energy of an Ru atom in the bulk metal, and <sup>b</sup> with respect to an isolated Ru atom.

To see what effect the adatom-vacancy mechanism has on the  $C_{60}$  structure, we simulated the  $C_{60}$  molecule on a 5-layer Ru(0001) substrate slab. There are a number of different ways in which  $C_{60}$  may sit on top the Ru substrate, and these orientations and their respective adsorption energies are listed in Table 1. The adsorption energies were calculated according to this formula:  $E_{ad} = E_{sys} - E_{slab} - E_{C60}$ , where  $E_{sys}$  is the energy of the system with  $C_{60}$  adsorbed on the Ru slab,  $E_{slab}$  is the energy of the pure Ru slab, and  $E_{C60}$  is the energy of the pure  $C_{60}$  molecule.  $C_{60}$  located at the on-top site is the most energetically favourable amongst configurations 1-4 in Table 1. If we remove the central Ru atom to form a Ru vacancy site (on-top\_vac configuration in Table 1), the adsorption energy of the system is now calculated as follows:  $E_{ad} = E_{sys} - E_{slab} - E_{C60} + \mu_{Ru}$ , where  $\mu_{Ru}$  is the chemical potential of the Ru atom that had been removed. The value of  $\mu_{Ru}$  is likely to be between that of bulk Ru and atomic Ru. Taking these two scenarios into account, the possible adsorption energy of the on-top\_vac configuration ranges from -9.077 eV (bulk Ru) to 1.361 eV (atomic Ru).

If we further consider the fact that vacancy formation is an entropically favorable process, the on-top\_vac system is certainly the most energetically favorable configuration.

## References

1. Marchini, S., Gunther, S. & Wintterlin, J. Scanning tunneling microscopy of graphene on Ru(0001). *Phys. Rev. B* **76**, 075429 (2007).
2. de Parga, A.L.V. et al. Periodically rippled graphene: Growth and spatially resolved electronic structure. *Phys. Rev. Lett.* **100**, 056807 (2008).
3. Martoccia, D. et al. Graphene on Ru(0001): A 25x25 supercell. *Phys. Rev. Lett.* **101**, 126102 (2008).
4. Pan, Y. et al. Highly Ordered, Millimeter-Scale, Continuous, Single-Crystalline Graphene Monolayer Formed on Ru (0001). *Adv. Mater.* **21**, 2777-2780 (2009).
5. Sutter, E., Acharya, D.P., Sadowski, J.T. & Sutter, P. Scanning tunneling microscopy on epitaxial bilayer graphene on ruthenium (0001). *Appl. Phys. Lett.* **94**, 133101 (2009).
6. Stolyarova, E. et al. High-resolution scanning tunneling microscopy imaging of mesoscopic graphene sheets on an insulating surface. *PNAS* **104**, 9209-9212 (2007).
7. Ishigami, M., Chen, J.H., Cullen, W.G., Fuhrer, M.S. & Williams, E.D. Atomic structure of graphene on SiO<sub>2</sub>. *Nano Lett.* **7**, 1643-1648 (2007).
8. Huang, H., Chen, W., Chen, S. & Wee, A.T.S. Bottom-up Growth of Epitaxial Graphene on 6H-SiC(0001). *Acs Nano* **2**, 2513-2518 (2008).
9. Xu, K., Cao, P.G. & Heath, J.R. Scanning Tunneling Microscopy Characterization of the Electrical Properties of Wrinkles in Exfoliated Graphene Monolayers. *Nano Lett.* **9**, 4446-4451 (2009).
10. Ritter, K.A. & Lyding, J.W. The influence of edge structure on the electronic properties of graphene quantum dots and nanoribbons. *Nature Mater.* **8**, 235-242 (2009).
11. Wang, W.L., Yazyev, O.V., Meng, S. & Kaxiras, E. Topological Frustration in Graphene Nanoflakes: Magnetic Order and Spin Logic Devices. *Phys. Rev. Lett.* **102**, 157201 (2009).
12. Kwon, S.Y. et al. Growth of Semiconducting Graphene on Palladium. *Nano Lett.* **9**, 3985-3990 (2009).
13. Schunack, M. et al. Long jumps in the surface diffusion of large molecules. *Phys. Rev. Lett.* **88**, 156102 (2002).
14. Somorjai, G.A., Contreras, A.M., Montano, M. & Rioux, R.M. Clusters, surfaces, and catalysis. *PNAS* **103**, 10577-10583 (2006).
15. Coraux, J. et al. Growth of graphene on Ir(111). *New J. Phys.* **11**, 023006 (2009).
16. Chen, H., Zhu, W.G. & Zhang, Z.Y. Contrasting Behavior of Carbon Nucleation in the Initial Stages of Graphene Epitaxial Growth on Stepped Metal Surfaces. *Phys. Rev. Lett.* **104**, 186101 (2010).